Materials Advances

ROYAL SOCIETY OF CHEMISTRY

COMMUNICATION

View Article Online
View Journal | View Issue

Check for updates

Cite this: *Mater. Adv.*, 2024, 5, 1022

Received 2nd December 2023,
Accepted 23rd December 2023

DOI: 10.1039/d3ma01080e

rsc.li/materials-advances

Alloy/strain engineering of Pt-based nanowires with controllable electronic structures towards boosted water electrolysis catalysis†

Jiakang Tian,‡[ade] Senmin Lin,‡[b] Zhongmin Tang,‡[b] Runhua Li,[ade] Xiaomei Cheng,[b] Zhen Fang,[ade] Bin Wang,[b] Jiaheng Peng,*[ade] Lang Xiao,[b] Benwei Fu,[a] Tao Deng *[ac] and Jianbo Wu *[abcde]

Low-dimensional platinum-based catalysts have aroused tremendous interest in electrocatalysis, benefiting from their high specific activity and novel electronic structures. Nevertheless, the practical application has been hampered by their complex synthesis process and finitely exposed active sites. Herein, we report novel 1D Pt-based nanowires (NWs) with inner tensile strain, multiple catalytically active lattice steps, and controllable electronic structures, which can be yielded through a facile large-scale room temperature reduction method on the gram scale. The favored geometrical and electronic structures are beneficial to improve the specific activity of catalytic sites towards boosting the water electrolysis process. By simply doping the second element (Ir or Ru) and inducing a tensile strain, the hydrogen evolution reaction (HER) can be substantially accelerated. In particular, PtIr-300 NWs/C showed an ultra-low overpotential of −9 mV and −18 mV at a current density of 10 mA cm^{-2} and 100 mA cm^{-2}. Additionally, PtIr-300 NWs/C attained 17.1-fold and 49.3-fold enhancement for the mass activity and intrinsic activity of HER recorded at 15 mV compared to Pt/C in 0.5 M H_2SO_4. This work paved a way to the design and construction of an efficient electrocatalyst.

Open Access Article. Published on 15 January 2024. Downloaded on 5/24/2026 2:44:20 AM.
This article is licensed under a Creative Commons Attribution-NonCommercial 3.0 Unported Licence.

Introduction

The total efficiency of energy conversion systems, such as water electrolysis, is severely constrained by the sluggish kinetics of the cathodic hydrogen evolution reaction (HER) and the anode oxygen evolution reaction (OER).[1–4] To date, electrocatalysts based on platinum group metals (PGM), including Pt, Ir, and Ru, have presented the most promising catalytic activity and durability for the HER and the OER. The PGM catalysts cannot be widely used as catalysts for water electrolysis due to their expensive cost and scarcity on Earth. Through strategies such as alloying,[5,6] surface straining,[7–11] and optimization of the coordination environments,[12–17] Pt-based nanocrystals not only achieve very high HER or OER activity in acidic media but also effectively reduce the use of precious metals. Alternatively, there are efforts to develop substitutive low-cost and high-performance catalysts to reduce the use of Pt-group metals.

In recent years, one-dimensional (1D) Pt-based nanowires (NWs) have provided an alternative approach to address the bottleneck of catalytic efficiency because of their out-bound intrinsic activity, fascinating properties, and promising applications in electrocatalysis.[18–29] Recent achievements indicated that strategies such as morphology engineering,[30–33] amorphization,[34] strain engineering,[35] defect engineering,[36] etc., can tune the surface electronic structures of metal catalysts, thus contributing to the optimization and improvement of the catalytic performance. For example, the strain on the surface changes the center position of the d-band relative to the catalyst Fermi level (ε_F), which in turn affects the adsorbate–catalyst surface interaction.[37] Furthermore, the band gaps of most 1D NWs can be tuned by inducing defects at the edges or the basal plane.[38–41] However, the efficiency of previously reported mono-enhancement strategy for 1D metal catalysts is barely satisfactory due to limited active sites and mass transfer. Moreover, conventional one-pot synthesis methods with the inevitable surfactant of syntheses in the liquid phase only have the rudimentary capability to synthesize trace amounts and hinder large-scale applications.[24,27] A large number of Pt-based high-activity HER catalysts doped with non-precious metals have been reported in recent years. However, it is difficult to achieve superior HER stability due to the huge electric potential gap between the non-precious metal elements and the Pt elements

[a] *State Key Laboratory of Metal Matrix Composites, School of Materials Science and Engineering, Shanghai Jiao Tong University, Shanghai 200240, P. R. China. E-mail: jianbowu@sjtu.edu.cn*
[b] *Emergency Rescue Center of Xinjiang Oilfield Company, China*
[c] *Center of Hydrogen Science, Shanghai Jiao Tong University, Shanghai 200240, P. R. China*
[d] *Materials Genome Initiative Center, Shanghai Jiao Tong University, Shanghai 200240, P. R. China*
[e] *Future Material Innovation Center, Zhangjiang Institute for Advanced Study, Shanghai Jiao Tong University, Shanghai 200240, P. R. China*

† Electronic supplementary information (ESI) available. See DOI: https://doi.org/10.1039/d3ma01080e

‡ These authors contributed equally to this paper.

© 2024 The Author(s). Published by the Royal Society of Chemistry

Open Access Article. Published on 15 January 2024. Downloaded on 5/24/2026 2:44:20 AM.
This article is licensed under a Creative Commons Attribution-NonCommercial 3.0 Unported Licence.

in acidic environments, which can easily lead to the collapse of the catalyst structure. In order to solve the above bottlenecks, alloy engineering coupled with strain engineering is adopted by inducing another element (Ir or Ru) and inner strain into 1D Pt-based NWs, which are beneficial to manipulate the electronic structure and enhance the intrinsic activity and long-term stability.[42]

Results and discussion

Herein, superfine 1D Pt-based nanowires (NWs) with Ir or Ru doping were yielded through a simple heat treatment under Ar/H_2 gas. For more information on synthesis methods (see the ESI†). It is worth remarking that the yield of PtIr NWs is about 0.25 g at a time (Fig. 1a), which is nearly one hundred times that of most of the reported noble metal-based nanomaterials prepared by the wet-chemical method.[27,29] Based on the experimental method, it can be anticipated that the yield would be further expanded if the number of precursors and the dimension of the synthetic reactor were further scaled up. To ascertain how the materials are affected by the temperature of synthesis, we compared the morphologies of PtIr NWs synthesized at 250, 300, 350, and 400 °C (PtIr-250 NWs, PtIr-300 NWs, PtIr-350 NWs, and PtIr-400 NWs). Fig. 1b shows the representative low-magnification transmission electron microscopy (TEM) image of PtIr-300 NWs, indicating that the resultant products were dominated by 1D nanowires. What is noticeable is that the PtIr-300 NWs exhibited very homogenous width distributions with sizes of *ca.* 4.2 nm (the corresponding illustration of Fig. 1b). Furthermore, we compared the morphological changes of PtIr-300 NWs at different temperatures. As shown in Fig. S1 (ESI†), the reduction temperature is controlled between 250 and 350 °C to maintain the NW morphology. When the temperature rises to 400 °C, significant agglomeration and growth of NWs occur. The selected area electron diffraction (SAED) pattern of Fig. 1b is composed of regular diffraction rings, which manifests that PtIr-300 NMs are in a face-centered cubic phase with dominant PtIr(111) and PtIr(200) facets (Fig. 1c). The diameters of the diffraction rings representing the (111) and (200) crystal planes are 8.79 nm^{-1} and 10.14 nm^{-1}, respectively, which is correlated with the spacing of the crystal planes in the corresponding materials. In addition, PtIr-350 NWs showed the similar diameter of 8.80 nm^{-1} and 10.10 nm^{-1} (Fig. S2a–c, ESI†), while PtIr-250 NWs and PtIr-400 NWs showed the larger diameters of 8.94 nm^{-1}/10.20 nm^{-1} (Fig. S3a–c, ESI†) and 8.91 nm^{-1}/10.22 nm^{-1} (Fig. S4a–c, ESI†), which represent the PtIr-300 NWs and PtIr-350 NWs might show tensile strain compared to PtIr-250 NWs and PtIr-400 NWs. As a comparison, Pt-300 NWs and PtRu-300 NWs were also synthesized by the same method and maintained similar NW morphology and lattice features, as shown in Fig. S5 and S6 (ESI†). In addition, Pt/Ir elements are uniformly distributed in the PtIr NWs, which is revealed by the STEM energy dispersive X-ray (STEM-EDX) elemental mapping (Fig. 1d). A similar result applies to PtRu NWs as well (Fig. 1e). The EDX spectrum and corresponding elemental quantification of PtIr NWs synthesized at different temperatures and PtRu NWs are represented in Fig. S7–S11 and Table S1 (ESI†). Note that both Ir and Ru achieved uniform doping and distribution under the above synthetic method. The X-ray diffraction (XRD) pattern in Fig. 1f confirms that the diffraction peaks of both PtIr-250 NWs, PtIr-300 NWs, PtIr-350 NWs, and PtIr-400 NWs were shifted positively *versus* Pt due to the lattice shrinkage caused by the alloying of Ir. The inset of Fig. 1f showed the locally enlarged spectra of the characteristic peaks of PtIr(111), and the peak positions of PtIr-250 NWs, PtIr-400 NWs, PtIr-350 NWs, and PtIr-300 NWs decreased sequentially (40.195/40.146/40.074/40.026), respectively, which show that their lattice spacings increased sequentially.

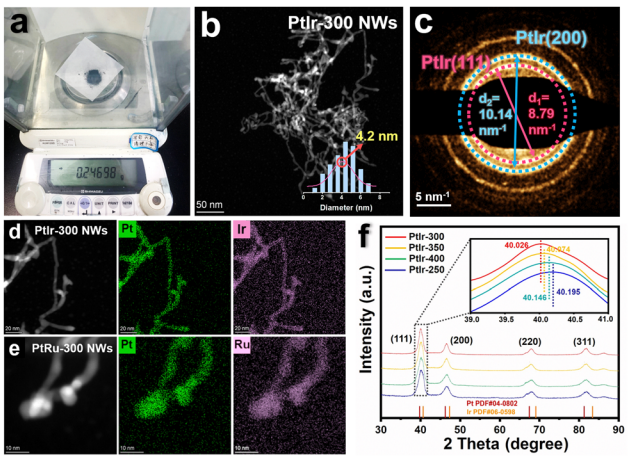

Fig. 1 The characterization of morphology and composition of PtIr-300 NWs. (a) Yield of PtIr NWs prepared in one batch. (b) Low-magnification TEM image. (c) The corresponding SAED image. STEM-EDX elemental mapping images of (d) PtIr-300 NWs and (e) PtRu-300 NWs, respectively. (f) XRD pattern of PtIr-250 NWs, PtIr-300 NWs, PtIr-350 NWs, and PtIr-400 NWs. The inset of locally enlarged spectra of the characteristic peaks of PtIr(111).

The entire structural characterization of PtIr NWs is shown in the high-resolution TEM (HRTEM) images with a lattice distance of *ca.* 1.81 Å for PtIr(200) facets and one of *ca.* 2.09 Å for PtIr(111) facets, respectively (Fig. 2a). It is worth noting that many atomic steps exist on an arbitrary exposed facet (Fig. 2b). The existence of these exposed straight crystal planes with atomic steps at the surface of the NWs fully exposes numerous unsaturated catalytically active sites that facilitate the water electrolysis process.[43–45] Furthermore, the structural characteristics of the tensile strain in PtIr NWs are examined using the geometrical phase analysis (GPA) technique. The resulting GPA maps (e_{yy}) clearly showed that there was a distinct distribution of lattice expansion in the PtIr NWs along the direction of PtIr(200) facets (Fig. 2c), while there was no expansion along the direction of e_{xx} (Fig. 2d). The comparison showed that there is a mass of lattice strain appeared along the PtIr NWs. The presence of inter lattice tensile strain and consequent variation in the electronic structure of the elements were further demonstrated by X-ray photoelectron spectroscopy (XPS). The Pt 4f (Fig. 2e) and Ir 4f (Fig. 2f) spectra both displayed double peaks that could be further decomposed into two asymmetric peaks.

© 2024 The Author(s). Published by the Royal Society of Chemistry

Open Access Article. Published on 15 January 2024. Downloaded on 5/24/2026 2:44:20 AM.
This article is licensed under a Creative Commons Attribution-NonCommercial 3.0 Unported Licence.

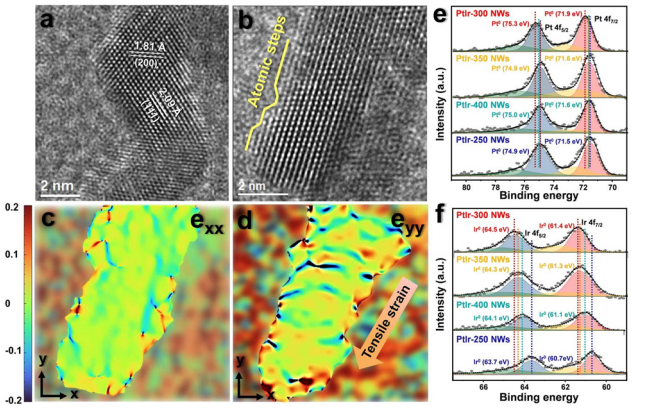

Fig. 2 The characterization of crystallographic and electronic structures of Ptlr NWs. (a) HRTEM image. (b) HRTEM image about the atomic steps and tensile strain in Ptlr-300 NWs. The GPA map along (c) e_{xx} and (d) e_{yy} about the HRTEM image of Ptlr NWs in Fig. 2b. The color-coded bar represents the −20% to +20% range. The (e) Pt 4f and (f) Ir 4f XPS spectra of Ptlr-250 NWs, Ptlr-300 NWs, Ptlr-350 NWs, and Ptlr-400 NWs.

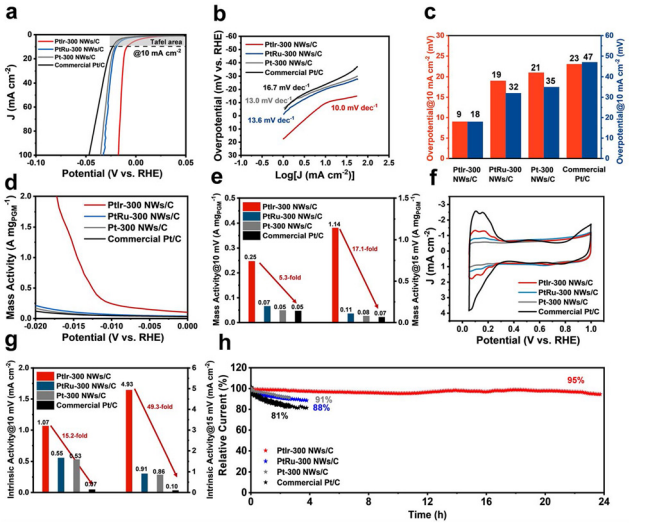

Fig. 3 Electrocatalytic performance of Ptlr-300 NWs/C, PtRu-300 NWs/C, Pt-300 NWs/C, and commercial Pt/C catalysts in 0.5 M H_2SO_4 electrolyte. (a) HER polarization curves at a scan rate of 5 mV s^{-1}. (b) The Tafel slopes. (c) Histogram of overpotentials at 10 mA cm^{-2} and 100 mA cm^{-2}. (d) Curve of mass activity *versus* overpotential. (e) Mass activity at an overpotential of 10 mV and 15 mV. (f) CV curves. (g) Intrinsic activity at an overpotential of 10 mV and 15 mV. (h) Chronoamperometric measurements.

In principle, the combination of the element Pt in a solid solution with another metallic element (M) of lower atomic number results in a positive shift of the Pt^0 peak towards higher binding energies, while the M^0 peak is negatively shifted.[35] For sample PtIr-250 NWs, the Pt $4f_{7/2}$ and Pt $4f_{5/2}$ binding energies (71.5 eV/74.9 eV) are both positively shifted by 0.5 eV *versus* the standard value (71.0 eV/74.4 eV) while the Ir $4f_{7/2}$ and Pt $4f_{5/2}$ binding energies (60.7 eV/63.7 eV) are both negatively shifted by 0.1 eV *versus* the standard value (60.8 eV/63.8 eV), which is consistent with the above principle. Interestingly, the Pt 4f and Ir 4f peaks of PtIr-300 NWs, PtIr-350 NWs, and PtIr-400 NWs were both positively shifted to varying degrees with respect to the standard values. With the $4f_{7/2}$ peaks as an example, the binding energy values of Pt^0/Ir^0 peaks for the PtIr-300 NWs, PtIr-350 NWs, and PtIr-400 NWs were 71.9 eV/61.4 eV, 71.6 eV/61.3 eV, and 71.6 eV/61.1 eV, and the values of positive shifts with respect to the standard value were recorded as 0.9 eV/0.7 eV, 0.6 eV/0.6 eV, and 0.6 eV/0.4 eV, respectively. For the PtIr NWs synthesized under different temperatures, the variation of the positive shift of the binding energy in the XPS 4f spectra matched the variation of the negative shift for the characteristic peak of PtIr(111) in the XRD spectra. Specifically, the electron density in the shell layers of Pt and Ir elements decreased gradually with the expansion of the lattice, which favored the head-to-head bonding with H* and enhanced the interaction of Pt–H and Ir–H, further boosting the HER performance.[35]

To investigate the effects of alloying, the electrocatalytic HER performance of PtIr and PtRu NWs synthesized at 300 °C was evaluated by a rotating disk electrode method. We also investigated Pt-300 NWs and commercial Pt/C catalysts. The as-synthesized Pt nanoparticles were supported onto the Vulcan XC-72R carbon with metal concentrations of 20 wt%. Fig. 3a depicted the corresponding polarization curves of PtIr-300, PtRu-300, Pt-300 NWs/C, and commercial Pt/C catalysts in 0.5 M H_2SO_4 electrolyte at a scan rate of 5 mV s^{-1}. The PtIr-300 NWs/C catalyst exhibits the smallest overpotential at a current density of 10 mA cm^{-2} and 100 mA cm^{-2} (−9 mV and −18 mV), which surpasses that of the other three catalysts (Fig. 3c and Table S2, ESI†) and offers great potential for practical applications in proton exchange membrane water electrolyzer (PEMWE). The Tafel slope, an important parameter for evaluating the catalyst HER kinetic process, was calculated for each sample based on the polarization curves (Fig. 3b). The Tafel slope of PtIr-300 NWs/C (10.0 mV dec^{-1}) is lower than those of PtRu-300 NWs/C (13.6 mV dec^{-1}), Pt-300 NWs/C (13.0 mV dec^{-1}), and commercial Pt/C (16.7 mV dec^{-1}) catalysts, indicating faster reaction paths and rate-determining steps, also suggesting the fast HER reaction kinetics on PtIr-300 NWs/C. The HER mass activity of the above catalysts was measured at 10 mV and 15 mV, respectively (Fig. 3c and d and Table S2, ESI†). PtIr-300 NWs/C showed the highest mass activity at both 10 mV and 15 mV, reaching 0.25 A mg_{PGM}^{-1} and 1.14 A mg_{PGM}^{-1}, which is 5.3 and 17.1 times higher than that of commercial Pt/C (0.05 A mg_{PGM}^{-1}/0.07 A mg_{PGM}^{-1}). Intrinsic activity calculated by normalizing the electrochemically specific area (ECSA) is commonly a realistic representation of the effect of atomic-scale modulation on catalysts. The ECSA of the above catalysts was calculated from the CV curves (Fig. 3f), and the intrinsic activities of the above catalysts were measured at 10 mV and 15 mV (Fig. 3g). PtIr-300 NWs/C showed the highest intrinsic activity at both 10 mV and 15 mV, reaching 1.07 mA cm^{-2} and 4.93 mA cm^{-2}, which is 15.2 and 49.3 times higher than that of commercial Pt/C (0.07 mA cm^{-2} and 0.10 mA cm^{-2}). Such a significant enhancement in the intrinsic activity of PtIr-300 NWs/C was attributed to the controllable preparation of the nanowire morphology and the doping of Ir elements. All the relevant performance index values for the above samples were all recorded

© 2024 The Author(s). Published by the Royal Society of Chemistry

Open Access Article. Published on 15 January 2024. Downloaded on 5/24/2026 2:44:20 AM.
This article is licensed under a Creative Commons Attribution-NonCommercial 3.0 Unported Licence.

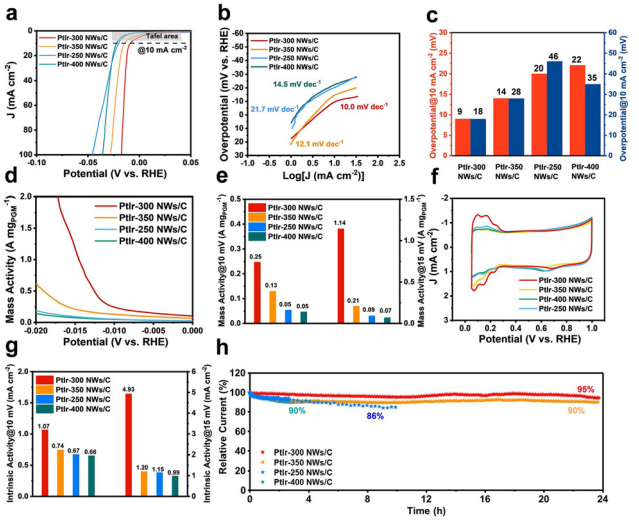

Fig. 4 Electrocatalytic performance of PtIr-300 NWs/C, PtIr-350 NWs/C, PtIr-250 NWs/C, and PtIr-400 NWs/C catalysts in 0.5 M H_2SO_4 electrolyte. (a) HER polarization curves at a scan rate of 5 mV s^{-1}. (b) The Tafel slopes. (c) Histogram of overpotentials at 10 mA cm^{-2} and 100 mA cm^{-2}. (d) Curve of mass activity *versus* overpotential. (e) Mass activity at an overpotential of 10 mV and 15 mV. (f) CV curves. (g) Intrinsic activity at an overpotential of 10 mV and 15 mV. (h) Chronoamperometric measurements.

in Table S2 (ESI†). Stability is another concern in electrocatalysts. Long-term chronoamperometric measurements (Fig. 3h) were performed on PtIr-300, PtRu-300, Pt-300 NWs/C, and commercial Pt/C electrodes. Only a 5% current density decay was recorded for the PtIr-300 NWs/C catalyst measured for 24 h, while the PtRu-300, Pt-300 NWs/C, and commercial Pt/C catalyst showed a significant decay of 12%, 9%, and 19% measured for less than 5 h, respectively. As displayed in Fig. S14 and Table S2 (ESI†), a negligible shift for the PtIr-300 NWs/C catalyst was observed after 24 h measured, demonstrating the superior long-term stability of the PtIr-300 NWs/C catalyst.

Furthermore, in order to explore the constitutive relationship between tensile strain and HER properties, the PtIr NWs synthesized at different temperatures (PtIr-250 NWs/C, PtIr-300 NWs/C, PtIr-350 NWs/C, and PtIr-400 NWs/C) were also investigated. The positive-going polarization curves of PtIr-250 NWs/C, PtIr-300 NWs/C, PtIr-350 NWs/C, and PtIr-400 NWs/C in 0.5 M H_2SO_4 electrolyte at a scan rate of 5 mV s^{-1} are recorded in Fig. 4a. The PtIr-300 NWs/C and PtIr-350 NWs/C with tensile strain exhibit the excellent performance of the top two (−9 mV @ 10 mA cm^{-2}/−18 mV @ 100 mA cm^{-2} and −14 mV @ 10 mA cm^{-2}/−28 mV @ 100 mA cm^{-2}), which surpasses PtIr-250 NWs/C and PtIr-400 NWs/C with a shorter lattice distance (Fig. 4c and Table S2, ESI†). The Tafel slopes at low overpotentials are 21.7, 10.0, 12.1, and 14.5 mV dec^{-1} for PtIr-250 NWs/C, PtIr-300 NWs/C, PtIr-350 NWs/C, and PtIr-400 NWs/C, respectively (Fig. 4b and Table S2, ESI†). PtIr-300 NWs/C still demonstrated the minimal Tafel slope value and a more positive onset potential, which indicated a faster reaction pathway and initiation of the response. The PtIr-300 NWs/C presented the highest mass activity (0.25 A mg_{PGM}^{-1}/1.14 A mg_{PGM}^{-1}) recorded at 10 mV and 15 mV (Fig. 4d and e and Table S2, ESI†) compared to PtIr-350 NWs/C (0.13 A mg_{PGM}^{-1}/0.21 A mg_{PGM}^{-1}), PtIr-250 NWs/C (0.05 A mg_{PGM}^{-1}/0.09 A mg_{PGM}^{-1}), and PtIr-400 NWs/C (0.05 A mg_{PGM}^{-1}/0.07 A mg_{PGM}^{-1}). The ECSA of PtIr-250 NWs/C, PtIr-300 NWs/C, PtIr-350 NWs/C, and PtIr-400 NWs/C were calculated from the CV curves (Fig. 4f). Benefiting from a maximum degree of tensile strain, the PtIr-300 NWs/C presented the highest intrinsic activity (1.07 mA cm^{-2}/4.93 mA cm^{-2}) recorded at 10 mV and 15 mV (Fig. 4g and Table S2, ESI†) compared to PtIr-350 NWs/C (0.74 mA cm^{-2}/1.20 mA cm^{-2}), PtIr-250 NWs/C (0.67 mA cm^{-2}/1.15 mA cm^{-2}), and PtIr-400 NWs/C (0.66 mA cm^{-2}/0.99 mA cm^{-2}). The long-term chronoamperometric measurements (Fig. 4h) were performed on PtIr-250 NWs/C, PtIr-300 NWs/C, PtIr-350 NWs/C, and PtIr-400 NWs/C electrodes. With the exception of the PtIr-300 NWs/C catalyst, which had a current density decay of only 5%, the PtIr-350 NWs/C catalyst also exhibited excellent stability with current density decays of 10% measured for 24 h. As shown in Fig. S15 and Table S2 (ESI†), negligible shifts for the PtIr-350 NWs/C catalyst were observed after a 24-hour measurement, demonstrating the superior long-term stability of PtIr-350 NWs/C catalysts. In addition, the nanowire morphology of PtIr-300 NWs/C and PtIr-350 NWs/C remained perfect after the long-term chronoamperometric testing for 24 h (Fig. S12 and S13, ESI†). Benefited from the perfect NW structure, PtIr-300 NWs/C and PtIr-350 NWs/C presented improved catalytic durability because of the improved resistance to the detachment from carbon support originating from the strengthened interaction between Pt-based NWs with carbon support.[46,47] Additionally, it can be seen from the TEM results that the unformed small particles still accumulate together due to the insufficient synthesis temperature of PtIr-250 NWs/C (Fig. S1a, ESI†), and the morphology of nanowires grows significantly due to the high synthesis temperature of PtIr-400 NWs/C (Fig. S1c, ESI†). These are the reasons for their poor stability.

Conclusions

In this work, the 1D Pt-based nanowires modulated by alloying and strain engineering were prepared through a large-scale reduction method. Attributed to the introduction of the Ir element, the PtIr-300 NWs/C catalyst exhibits the smallest overpotential at a current density of 10 mA cm^{-2} and 100 mA cm^{-2} (−9 mV and −18 mV *versus* RHE), which surpasses the PtRu-300 NWs/C (−19 mV and −32 mV *versus* RHE), Pt-300 NWs/C (−21 mV and −35 mV *versus* RHE), and commercial Pt/C catalysts (−23 mV and −47 mV *versus* RHE). Furthermore, the degree of strain in the PtIr NWs was modulated by controlling the reduction temperature. The PtIr-300 NWs exhibited the perfect nanowire morphology, exhibited maximum lattice strain, and showed an optimal HER performance under 300 °C synthesis conditions. This research introduces an ingenious synthetic approach for low-dimensional Pt-based catalysts, which will open up new opportunities for the practical application of noble metal-based nanocatalysts.

© 2024 The Author(s). Published by the Royal Society of Chemistry

Open Access Article. Published on 15 January 2024. Downloaded on 5/24/2026 2:44:20 AM. This article is licensed under a Creative Commons Attribution-NonCommercial 3.0 Unported Licence.

Author contributions

Jiakang Tian: data curation, investigation, and writing – original draft. Senmin Lin: data curation, investigation, and writing – original draft. Zhongmin Tang: data curation, investigation, and writing – original draft. Runhua Li: investigation and validation. Xiaomei Cheng: investigation and validation. Zhen Fang: investigation and validation. Bin Wang: investigation and validation. Jiaheng Peng: conceptualization, supervision, and writing – review & editing. Lang Xiao: investigation and validation. Benwei Fu: investigation and validation. Tao Deng: conceptualization, funding acquisition, supervision, and writing – review & editing. Jianbo Wu: conceptualization, funding acquisition, supervision, and writing – review & editing.

Conflicts of interest

There are no conflicts to declare.

Acknowledgements

This work was sponsored by the National Natural Science Foundation of China (21875137, 51521004, and 51420105009). The authors thank the Program of Shanghai Academic/Technology Research Leader (Project No. 23XD1422100), the Innovation Program of Shanghai Municipal Education Commission (2019-01-07-00-02-E00069), the 111 Project (B16032), the Research and application of integrated technology for hydrogen production by water electrolysis and hydrogen storage (20221504350300), and the Center of Hydrogen Science and Joint Research Center for Clean Energy Materials at Shanghai Jiao Tong University for financial support.

Notes and references

1 C. V. Pham, D. Escalera-López, K. Mayrhofer, S. Cherevko and S. Thiele, *Adv. Energy Mater.*, 2021, **11**, 2101998.
2 C. Spori, J. T. H. Kwan, A. Bonakdarpour, D. P. Wilkinson and P. Strasser, *Angew. Chem., Int. Ed.*, 2017, **56**, 5994–6021.
3 A. Z. Tomić, I. Pivac and F. Barbir, *J. Power Sources*, 2023, **557**, 232569.
4 S. Shit, S. Bolar, N. C. Murmu and T. Kuila, *Chem. Eng. J.*, 2022, **428**, 131131.
5 Y. Xu and B. Zhang, *Chem. Soc. Rev.*, 2014, **43**, 2439–2450.
6 H. Zhang, M. Jin and Y. Xia, *Chem. Soc. Rev.*, 2012, **41**, 8035–8049.
7 J. Li, E. Liu, S. Hwang, S. Mukerjee and Q. Jia, *ACS Catal.*, 2021, **11**, 8165–8173.
8 Y. Guo, B. Hou, X. Cui, X. Liu, X. Tong and N. Yang, *Adv. Energy Mater.*, 2022, **12**, 2201548.
9 H. Xie, S. Chen, J. Liang, T. Wang, Z. Hou, H.-L. Wang, G. Chai and Q. Li, *Adv. Funct. Mater.*, 2021, **31**, 2100883.
10 A. Alinezhad, L. Gloag, T. M. Benedetti, S. Cheong, R. F. Webster, M. Roelsgaard, B. B. Iversen, W. Schuhmann, J. J. Gooding and R. D. Tilley, *J. Am. Chem. Soc.*, 2019, **141**, 16202–16207.
11 J. Kim, H. Kim, W.-J. Lee, B. Ruqia, H. Baik, H.-S. Oh, S.-M. Paek, H.-K. Lim, C. H. Choi and S.-I. Choi, *J. Am. Chem. Soc.*, 2019, **141**, 18256–18263.
12 F.-Y. Yu, Z.-L. Lang, Y.-J. Zhou, K. Feng, H.-Q. Tan, J. Zhong, S.-T. Lee, Z.-H. Kang and Y.-G. Li, *ACS Energy Lett.*, 2021, **6**, 4055–4062.
13 H. Jin, M. Ha, M. G. Kim, J. H. Lee and K. S. Kim, *Adv. Energy Mater.*, 2023, **13**, 2204213.
14 Z. Wang, B. Xiao, Z. Lin, Y. Xu, Y. Lin, F. Meng, Q. Zhang, L. Gu, B. Fang, S. Guo and W. Zhong, *Angew. Chem., Int. Ed.*, 2021, **60**, 23388–23393.
15 X. Zheng, P. Cui, Y. Qian, G. Zhao, X. Zheng, X. Xu, Z. Cheng, Y. Liu, S. X. Dou and W. Sun, *Angew. Chem., Int. Ed.*, 2020, **59**, 14533–14540.
16 X. Cheng, Y. Lu, L. Zheng, M. Pupucevski, H. Li, G. Chen, S. Sun and G. Wu, *Mater. Today Energy*, 2021, **20**, 100653.
17 X. Cheng, Y. Lu, L. Zheng, Y. Cui, M. Niibe, T. Tokushima, H. Li, Y. Zhang, G. Chen, S. Sun and J. Zhang, *Nano Energy*, 2020, **73**, 104739.
18 Y. Zhu, L. Bu, Q. Shao and X. Huang, *ACS Catal.*, 2019, **9**, 6607–6612.
19 B. Y. Xia, H. B. Wu, N. Li, Y. Yan, X. W. Lou and X. Wang, *Angew. Chem., Int. Ed.*, 2015, **54**, 3797–3801.
20 W. Tong, B. Huang, P. Wang, Q. Shao and X. Huang, *Natl. Sci. Rev.*, 2021, **8**, nwaa088.
21 H. Jin, Z. Xu, Z.-Y. Hu, Z. Yin, Z. Wang, Z. Deng, P. Wei, S. Feng, S. Dong, J. Liu, S. Luo, Z. Qiu, L. Zhou, L. Mai, B.-L. Su, D. Zhao and Y. Liu, *Nat. Commun.*, 2023, **14**, 1518.
22 Y. Liu, Y. Zhang, H. Hua and Y. Li, *RSC Adv.*, 2017, **7**, 44552–44558.
23 H. Li, X. Wu, X. Tao, Y. Lu and Y. Wang, *Small*, 2020, **16**, 2001135.
24 E. B. Tetteh, C. Gyan-Barimah, H.-Y. Lee, T.-H. Kang, S. Kang, S. Ringe and J.-S. Yu, *ACS Appl. Mater. Interfaces*, 2022, **14**, 25246–25256.
25 F. S. M. Ali, R. L. Arevalo, M. Vandichel, F. Speck, E.-L. Rautama, H. Jiang, O. Sorsa, K. Mustonen, S. Cherevko and T. Kallio, *Appl. Catal., B*, 2022, **315**, 121541.
26 T. Rajala, R. Kronberg, R. Backhouse, M. E. M. Buan, M. Tripathi, A. Zitolo, H. Jiang, K. Laasonen, T. Susi, F. Jaouen and T. Kallio, *Appl. Catal., B*, 2020, **265**, 118582.
27 K. Yin, Y. Chao, F. Lv, L. Tao, W. Zhang, S. Lu, M. Li, Q. Zhang, L. Gu, H. Li and S. Guo, *J. Am. Chem. Soc.*, 2021, **143**, 10822–10827.
28 M. Wang, M. Wang, C. Zhan, H. Geng, Y. Li, X. Huang and L. Bu, *J. Mater. Chem. A*, 2022, **10**, 18972–18977.
29 H. Huang, L. Fu, W. Kong, H. Ma, X. Zhang, J. Cai, S. Wang, Z. Xie and S. Xie, *Small*, 2022, **18**, e2201333.
30 Z. He, L. G. Chang, Y. Lin, F. L. Shi, Z. D. Li, J. L. Wang, Y. Li, R. Wang, Q. X. Chen, Y. Y. Lu, Q. H. Zhang, L. Gu, Y. Ni, J. W. Liu, J. B. Wu and S. H. Yu, *J. Am. Chem. Soc.*, 2020, **142**, 7968–7975.
31 T. He, W. Wang, X. Yang, F. Shi, Z. Ye, Y. Zheng, F. Li, J. Wu, Y. Yin and M. Jin, *ACS Nano*, 2021, **15**, 7348–7356.
32 S. Muhamed, R. K. Aparna, A. Karmakar, S. Kundu and S. Mandal, *Inorg. Chem.*, 2023, **62**, 7195–7202.

© 2024 The Author(s). Published by the Royal Society of Chemistry

Open Access Article. Published on 15 January 2024. Downloaded on 5/24/2026 2:44:20 AM.
This article is licensed under a Creative Commons Attribution-NonCommercial 3.0 Unported Licence.

33 R. K. Aparna, A. Karmakar, R. T. Arsha, S. Kundu and S. Mandal, *Chem. Commun.*, 2023, **59**, 10444–10447.
34 J. Tian, Y. Shen, P. Liu, H. Zhang, B. Xu, Y. Song, J. Liang and J. Guo, *J. Mater. Sci. Technol.*, 2022, **127**, 1–18.
35 H. Guo, L. Li, Y. Chen, W. Zhang, C. Shang, X. Cao, M. Li, Q. Zhang, H. Tan, Y. Nie, L. Gu and S. Guo, *Adv. Mater.*, 2023, **35**, 2302285.
36 S. Gratious, A. Karmakar, D. Kumar, S. Kundu, S. Chakraborty and S. Mandal, *Nanoscale*, 2022, **14**, 7919–7926.
37 S. Zhang, X. Zhang, G. Jiang, H. Zhu, S. Guo, D. Su, G. Lu and S. Sun, *J. Am. Chem. Soc.*, 2014, **136**, 7734–7739.
38 F. Lin, F. Lv, Q. Zhang, H. Luo, K. Wang, J. Zhou, W. Zhang, W. Zhang, D. Wang, L. Gu and S. Guo, *Adv. Mater.*, 2022, **34**, 2202084.
39 Y. Zuo, D. Rao, S. Li, T. Li, G. Zhu, S. Chen, L. Song, Y. Chai and H. Han, *Adv. Mater.*, 2018, **30**, 1704171.
40 X. Mu, J. Gu, F. Feng, Z. Xiao, C. Chen, S. Liu and S. Mu, *Adv. Sci.*, 2021, **8**, 2002341.
41 Y. Chen, J. Pei, Z. Chen, A. Li, S. Ji, H. Rong, Q. Xu, T. Wang, A. Zhang, H. Tang, J. Zhu, X. Han, Z. Zhuang, G. Zhou and D. Wang, *Nano Lett.*, 2022, **22**, 7563–7571.
42 L. Li and Y. Ji, *Small*, 2021, **17**, 2103798.
43 Z. Liu, G. Zhang, J. Bu, W. Ma, B. Yang, H. Zhong, S. Li, T. Wang and J. Zhang, *ACS Appl. Mater. Interfaces*, 2020, **12**, 36259–36267.
44 Z. Kou, K. Xi, Z. Pu and S. Mu, *Nano Energy*, 2017, **36**, 374–380.
45 J. Yang, C. Lei, H. Wang, B. Yang, Z. Li, M. Qiu, X. Zhuang, C. Yuan, L. Lei, Y. Hou and X. Feng, *Nanoscale*, 2019, **11**, 17571–17578.
46 K. Li, X. Li, H. Huang, L. Luo, X. Li, X. Yan, C. Ma, R. Si, J. Yang and J. Zeng, *J. Am. Chem. Soc.*, 2018, **140**, 16159–16167.
47 C. Wang, Y. Hou, J. Kim and S. Sun, *Angew. Chem., Int. Ed.*, 2007, **46**, 6333–6335.

© 2024 The Author(s). Published by the Royal Society of Chemistry